PCCP

ROYAL SOCIETY OF CHEMISTRY

PAPER

View Article Online
View Journal | View Issue



Cite this: *Phys. Chem. Chem. Phys.*, 2024, **26**, 4898

# Theoretical study of the effects of alloying elements on $TiO_2/Ti_2AlNb$ interface adhesion properties†

Y. Li,[a] B. Shi, *[b] J. H. Dai*[a] and Y. Song [a]

Received 28th September 2023,
Accepted 12th January 2024

DOI: 10.1039/d3cp04727j

rsc.li/pccp

$Ti_2AlNb$-based alloys are expected to be applied in the manufacture of parts of aeroengines to achieve the goal of increasing the thrust-to-weight ratio. However, the poor high temperature oxidation resistance of these alloys may hinder their applications. Alloying has been proven to be effective in improving oxidation resistance properties. However, the selection of alloying elements and their influence mechanisms are rarely studied. The $TiO_2/Ti_2AlNb$ interface bonding interactions and the effects of alloying elements of Si, Sc, Y, Zr, Mo and Hf were investigated *via* first principles calculations. The separation energy and electronic structure were studied to explore the bonding interactions between the oxide scale and $Ti_2AlNb$ matrix. When Zr and Hf are used to replace Al, the bonding properties of the $TiO_2/Ti_2AlNb$ interface are improved. The tensile and shear deformations of the interfacial zones are applied to study the influence of alloying elements on the $TiO_2$ oxide spalling on $Ti_2AlNb$. The tensile strength is increased by more than 2 GPa when Nb is substituted by the Sc, Zr and Hf elements. Therefore, Sc, Zr, and Hf are beneficial for inhibiting oxide spalling and will have great potential to improve the oxidation resistance properties.



## 1 Introduction

$Ti_2AlNb$-based alloys have the characteristics of high specific strength, good high-temperature fracture toughness, and strong creep resistance. They show broad application prospects in the aviation field. Compared with traditional Ti alloys, they have higher aluminum contents[1,2] and can be used to achieve the effect of improving the thrust-to-weight ratio of aeroengines.[3] However, there are also some defects that hinder their practical application, among which the insufficient oxidation resistance is one of the most critical issues. Due to the bonding competition between O–Ti and O–Al at high temperatures,[4] mixed oxides such as $TiO_2$ and $Al_2O_3$ appear during the oxidation process. The irregular oxide layer cannot protect the matrix and accelerates the oxidation process of the alloys. Oxidation behavior can damage the mechanical properties of the alloys and even lead to failure.[5] During the oxidation process, hetero-structure interfaces between the matrix and the oxide are formed, which become the weakest areas. It is easy to produce interface cracking under the action of stress, resulting in structural failure, which will have a serious impact on the service life of the alloys. Research on the adhesion properties of oxides on the substrate is necessary for the reliable design and application of the $Ti_2AlNb$-based alloys.

Theoretical calculations can simulate the normal separation process of the interface at the atomic scale. By applying strain between surface slabs, the strength and fracture mechanism of the interface can be analyzed, which can provide a reference for the analysis of the spalling of the oxides.[6–10] On the other hand, by simulating the sliding barrier, the tangential separation behavior of the interface system can be studied. The tangential stress, which is required to overcome the potential barrier and maintain sliding within the surface slabs, can be used to evaluate the shear resistance of the interface. The lower the energy consumed by sliding, the worse the interface stability and resistance to tangential separation.[11–14]

For Ti–Al alloys, we studied the stability and oxide adhesion properties of γ-TiAl/$Al_2O_3$ and γ-TiAl/$TiO_2$ interfaces.[15–18] By calculating the effects of different stacking forms and relative positions on stability, we found that $Al_2O_3$ and $TiO_2$ tend to combine with Al and Ti atoms on the surface of the γ-TiAl alloy, respectively. Alloying elements and defects will affect the strength of the interface. For the $TiO_2$/TiAl interface, Y, Nb and Pd could increase the strength and help preventing spalling of the oxide. For the $Al_2O_3$/TiAl interface system, the

[a] *School of Materials Science and Engineering, Harbin Institute of Technology at Weihai, 2 West Wenhua Road, Weihai, 264209, China. E-mail: daijh@hit.edu.cn*
[b] *Shandong Provincial Key Lab of Special Welding Technology, Harbin Institute of Technology at Weihai, 2 West Wenhua Road, Weihai, 264209, China. E-mail: shibin@hit.edu.cn*

† Electronic supplementary information (ESI) available. See DOI: https://doi.org/10.1039/d3cp04727j

influence of alloying elements on the γ-TiAl/$Al_2O_3$ interaction is limited. However, alloying greatly improves the adhesion strength of the α2-$Ti_3Al$/$Al_2O_3$ interface. The increase of strength may be due to the strong interaction between the alloying elements and $Al_2O_3$. Other research reports also show that elements such as Mo will reduce the adhesion energy of the $TiO_2$/γ-TiAl interface and have a negative impact.[19] The doping of B can significantly enhance the strength of the $Al_2O_3$/γ-TiAl interface, while the effect of Nb on the strength of the $TiO_2$/γ-TiAl interface is not obvious.[20,21] The presence of P element will reduce the bonding strength of the TiAl/$Ti_3Al$ interface, because P more easily combines with Ti, resulting in the weakening of Ti–Al bonding. This indicates that the addition of P has a negative impact on the plasticity of the TiAl/$Ti_3Al$ interface.[22] In summary, alloying elements can affect the stability and adhesion properties of the interface.

The stacking form of the interface and the electronic structure at the interface are the most important factors affecting its stability and adhesion properties. For the TiAl/$Ti_2AlNb$ interface, the bond strength at the interface decreases in the order of Ti–Nb > Ti–Al > Nb–Al, and the interface bonding is enhanced through electron redistribution and hybridization of d and p electrons.[23,24] For the Ti(0001)/$TiAl_3$(110) interface, the HCP stacking system has the highest work of separation among various stacking forms. Further, interface fracture toughness calculation results show that the HCP interface structure has the greatest degree of atomic interaction and the largest degree of charge transfer, due to the hybridization of the d electron orbital of the Ti atom and the p electron orbital of the Al atom, which are the main factors that strengthen the adhesion properties of the interface.[25]

We have previously studied the stability of the low-index surface of $Ti_2AlNb$ and the adsorption performance of oxygen atoms on the $Ti_2AlNb$ surface and found that the mixed terminal surface of Al, Ti, and Nb elements has good stability. When oxygen atoms are adsorbed, they are well bonded with Ti atoms and tend to form titanium oxides.[26] The oxidation products of the $Ti_2AlNb$ alloy are mainly $TiO_2$ and $AlNbO_4$, while $Al_2O_3$ mainly exists as an intermediate product.[27] Although the Ti element competes with Al and Nb elements in the oxidation process, the increase in oxygen partial pressure is conducive to the formation of $TiO_2$.[28,29] This paper studies the effect of alloying on the adhesion properties of $TiO_2$ on the $Ti_2AlNb$ matrix.

## 2. Computational details

The Vienna Ab initio Simulation Packages (VASP) are employed to explore the interface structures and their stabilities.[30] The generalized gradient approximation (GGA) with the Perdew–Burke–Ernzerhof (PBE) functional was chosen to consider the exchange–correlation interactions of the studied systems.[31] (The PBE functional has been proven to be more accurate in first-principles calculation studies of $Ti_2AlNb$ and γ-TiAl systems as shown in ref. 24, 32 and 33.) Projector augmented wave (PAW) pseudopotentials are used in the present study.[34] The *k*-mesh and cutoff energy were tested respectively, and the results

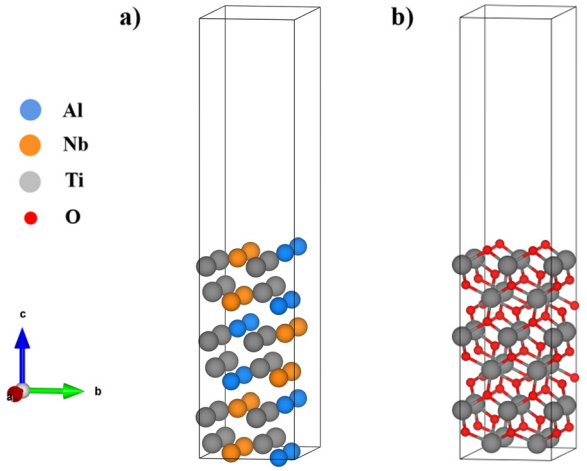


Fig. 1 (a) $Ti_2AlNb$(010) surface and (b) $TiO_2$(001) surface.

are shown in Fig. S1 (ESI†). A cutoff energy of 500 eV is selected for the plane wave basis set. The *k*-mesh is set to 3 × 4 × 1. The total energy convergence is 0.1 meV per cell, and the structural optimization was stopped when the force on every atom was smaller than 0.01 eV $Å^{-1}$. Considering the metallic properties of studied interface systems, the method of Methfessel–Paxton order 1 is used in the self-consistent calculation to improve the convergence velocity.

The O-phase $Ti_2AlNb$ surface model uses a 2 × 2 supercell of the (010) surface,[26] containing a total of 6 atomic layers and 48 atoms. Fig. 1(a) shows the structure of the $Ti_2AlNb$ surface and the lattice parameters are $a$ = 9.34 and $b$ = 6.05. The rutile $TiO_2$(001) surface with a 2 × 2 supercell is chosen to simulate the oxide scale. The $TiO_2$ structure is shown in Fig. 1(b): $a$ = 9.19 Å and $b$ = 5.92 Å, containing a total of 6 Ti atomic layers and 12 O atomic layers. The lattice mismatch between the $Ti_2AlNb$ matrix and rutile $TiO_2$ is 2.1%. In order to prevent interatomic interactions caused by periodicity, a vacuum layer of 15 Å is added.

## 3. Results and discussion

### 3.1 Stability of the alloying element containing $TiO_2$/$Ti_2AlNb$ interface

Previously, we studied the bonding properties of the $TiO_2$/γ-TiAl interface. It was found that the interface with a smaller mismatch degree has stronger stability, and the stacking form was found to have a greater impact on the stability of the interface.[15,16] To establish the $TiO_2$/$Ti_2AlNb$ interface structures, different stacking models were considered. Due to the high symmetry of the $TiO_2$(110) surface, the O phase (010) surface is chosen as the base surface, and different stacking models are established by adjusting the positions of $TiO_2$ terminal atoms, as shown in Fig. 2. When the terminal oxygen atom of $TiO_2$ is located directly above the Ti atom on the surface of $Ti_2AlNb$, the stacking form is labelled as OT-1. When the oxygen atom is located directly above the Al and Nb atoms, the stacking form is then labelled as OT-2. The oxygen position directly located above the center of Al and Ti atoms is marked as bridge. When the oxygen atom is located

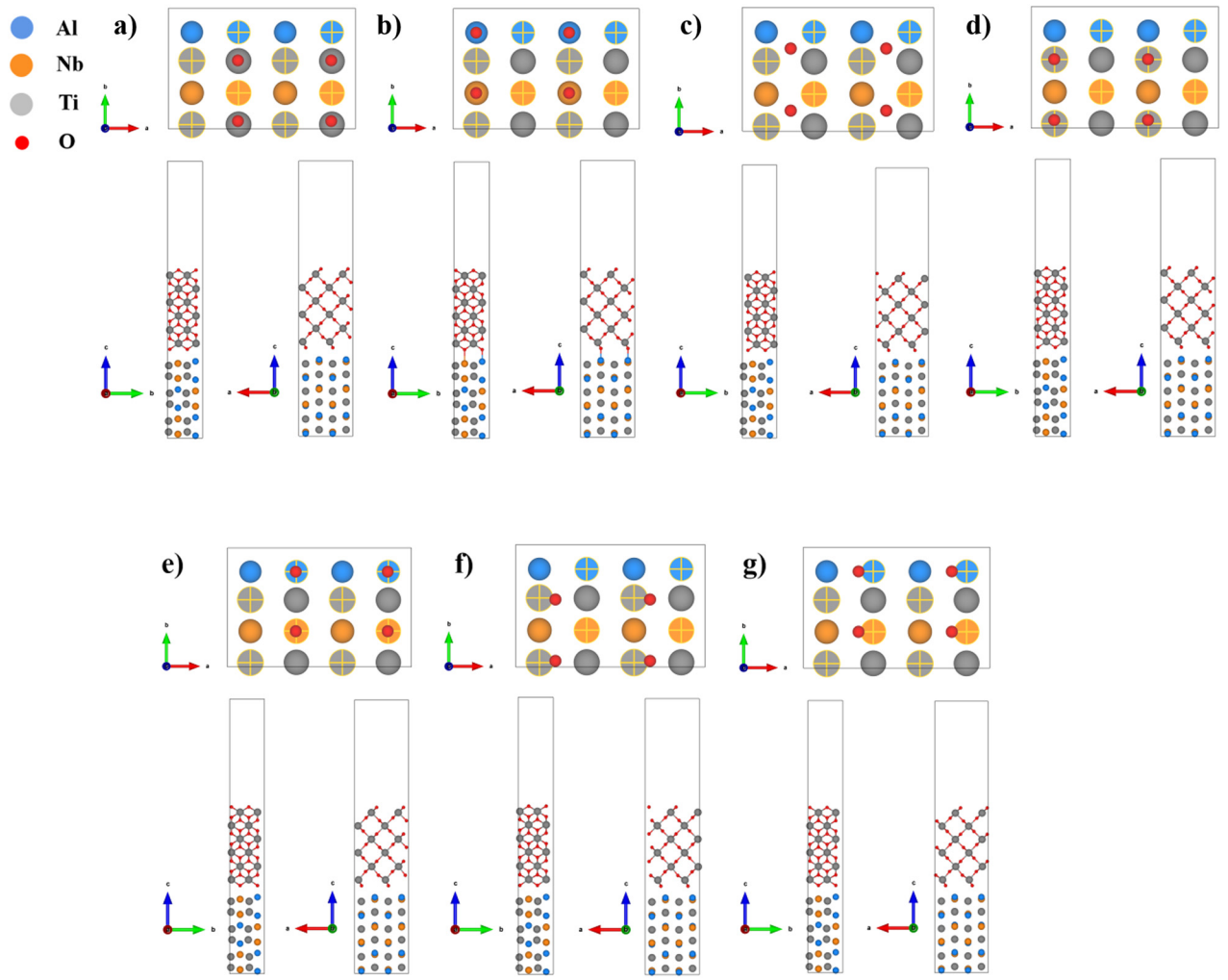


Fig. 2 Stacking forms of the $TiO_2/Ti_2AlNb$ interface: (a) OT-1, (b) OT-2, (c) bridge, (d) HCP-1, (e) HCP-2, (f) FCC-1, and (g) FCC-2.

directly above the Ti atom of the $Ti_2AlNb$ subsurface layer or directly above the Al and Nb atoms, the stacking forms are labelled as HCP-1 and HCP-2, respectively. Similarly, two other FCC positions are also selected to construct the interface model. The interface stability also changes with the interface spacing. Various interface spacings are set for each stacking structure, ranging from 0.5 Å to 4.5 Å.

In order to obtain the ideal interface spacing of each stacking interface, the universal binding energy relation (UBER) curve proposed by Rose *et al.* was used to fit the relationship between energy and interface spacing.[35] The formula is as follows:

$$E_{\text{form}} = -\Delta E\left(1 + \frac{d - d_0}{l}\right)\exp\left(-\frac{d - d_0}{l}\right) \quad (1)$$

where $E_{\text{form}}$ is the interface formation energy under equilibrium conditions, $d$ is the interface spacing, $d_0$ is the equilibrium value, that is, the ideal interface spacing, and $l$ is the Thomas–Fermi value specific to the material on each side of the interface. The calculation formula of the formation energy $E_{\text{form}}$ is defined as follows:

$$E_{\text{form}} = (E_{TiO_2/Ti_2AlNb} - E_{Ti_2AlNb} - E_{TiO_2})/A \quad (2)$$

In the above formula, the $E_{TiO_2/Ti_2AlNb}$, $E_{Ti_2AlNb}$ and $E_{TiO_2}$ are the energies of the interface, O phase surface and $TiO_2$ surface system respectively. The UBER curve describes the bonding force between two rigid atomic planes, and the energy and structure are obtained without relaxation. The $k$-mesh of the system is set to $3 \times 4 \times 1$.

The UBER fitting curve and interface spacing are shown in Fig. 3 and Table 1, respectively. After UBER fitting, the $d_0$ of each stacking form is obtained, and the formation energy of the interface is calculated from the interface spacing $d_0$. The interface model was re-established using the fitted interface spacing. Three layers of atoms on the top and bottom of the interface model were fixed, and other six layers of atoms were optimized. After optimization, the formation energy of the interface is calculated according to formula (2). The results are shown in Table 1. The formation energy of HCP-2 is the lowest, $-2.39$ J m$^{-2}$, indicating that this stacking form is the most stable. The interface of γ-TiAl with both $TiO_2$ and $Al_2O_3$ shows the negative formation energies of the most stable

 

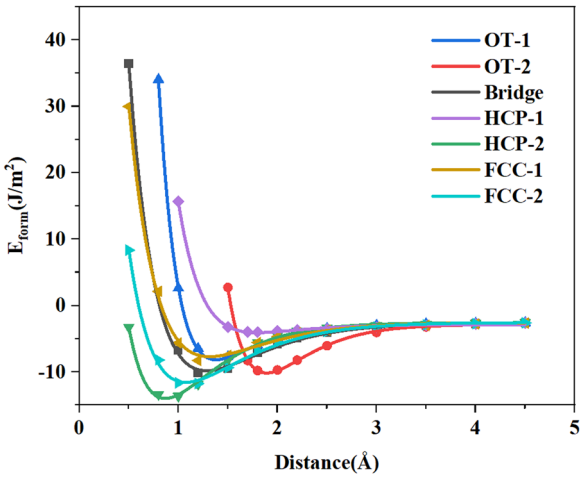


Fig. 3 UBER fitting $E_{form}$–distance curves of the $TiO_2/Ti_2AlNb$ interface (the abscissa corresponding to the lowest point of each curve is $d_0$ obtained by fitting).

Table 1 Interfacial spacing and formation energies of each stacking form of the $TiO_2/Ti_2AlNb$ interface

| | $d_0$ (Å) | $E_{form}$ (J m$^{-2}$) |
|---|---|---|
| OT-1 | 1.38 | −1.85 |
| OT-2 | 1.89 | −1.37 |
| Bridge | 1.28 | −1.96 |
| HCP-1 | 1.80 | −1.55 |
| HCP-2 | 0.87 | −2.39 |
| FCC-1 | 1.30 | −1.98 |
| FCC-2 | 1.07 | −2.19 |

stacking forms, which are consistent with the calculation results of this article.[15–17] Furthermore, Bakulin's research studies also showed similar results.[36,37]

Based on the stable $TiO_2/Ti_2AlNb$ interface model, the alloying elements of Si, Sc, Y, Zr, Mo and Hf are further considered to study their influence on the stability properties of the interface. The selection of these alloying elements is mainly based on existing experimental reports. Si, Zr and Mo have been confirmed by relevant experiments to promote the oxidation resistance of $Ti_2AlNb$,[38–40] and the Y element has also been used as the anti-oxidation modification element in TiAl alloys. There are few studies on the influence of Sc and Hf on the oxidation properties of alloys, but the Hf element can work together with the Zr element to improve the creep resistance of γ-TiAl.[41] With a small mass density, Sc comes from the same period as the Ti element and also belongs to the same family as the Y element. Therefore, these alloying elements are selected to study their effects on the interface adhesion properties. Each alloying element is used to substitute the three elements of Al, Ti, and Nb in the O phase of the $Ti_2AlNb$ surface layer in the interface, and the structure is then optimized to obtain a stable alloyed interface model. First, the substitution stability of alloying elements was calculated according to the following formula:

$$E_{occu} = E_{TiO_2/Ti_2AlNb-X} - E_{TiO_2/Ti_2AlNb} + E_M - E_X \quad (3)$$

Table 2 Formation energies (eV) of the doped alloying elements on the O phase (010)-c surface

| Alloying elements | Al | Nb | Ti |
|---|---|---|---|
| Si | −0.02 | −0.23 | 0.39 |
| Sc | −0.50 | −1.05 | 0.25 |
| Y | 0.27 | −0.43 | 1.73 |
| Zr | −0.12 | −0.69 | 0.64 |
| Mo | 1.58 | 0.10 | 1.06 |
| Hf | −0.17 | −0.54 | 0.66 |

In the above formula, $E_{TiO_2/Ti_2AlNb-X}$, $E_{TiO_2/Ti_2AlNb}$, $E_M$, and $E_X$ are the energies of the interface after alloying with selected elements, the original interface, the substituted atoms (Al, Ti, and Nb atoms), and the alloying atoms, respectively. The calculated occupation energies are shown in Table 2. It can be seen that the Nb substituted systems are more stable than the other two substituted systems, and all the elements except Mo have negative occupation energies. Therefore, most interface models should be more stable compared with the bare interface.

In the Al substituted system, as shown in Fig. 4, the Si and Mo atoms move downward after relaxation and far away from oxygen atoms, while the Sc, Y, Zr, and Hf atoms basically maintain their original positions and therefore strongly bond with oxygen atoms. In the Ti substituted system, as shown in Fig. 5, the Si atoms move downward relative to the original position after relaxation and therefore bond with different oxygen atoms. Affected by the movement of Si atoms, some Ti and oxygen atoms of $TiO_2$ also move downward, which cause large distortions. The other alloying elements basically maintain their original positions and should have strong bonding interactions with oxygen atoms. In the Nb substituted system, as shown in Fig. 6, the Si and Mo atoms move downward from their original positions and bond with different oxygen atoms, while the Sc, Y, Zr and Hf atoms basically maintain their original positions (Table 3).

### 3.2 Interface adhesion performance

To simulate the normal separation process, the interfacial spacing between the $TiO_2$ and $Ti_2AlNb$ slabs was gradually changed along the *c*-axis from −0.4 Å to 4.0 Å. The rigid shift is adopted during the normal separation process,[8,42] in which the atomic positions along *a* and *b* axes are fixed.

The interface separation work is calculated using eqn (4). The work of separation is defined as the energy difference between the interface system and the isolated surface model in the system,

$$W_{sep} = (E_{Ti_2AlNb} + E_{TiO_2} - E_{Ti_2AlNb/TiO_2})/A \quad (4)$$

where $E_{Ti_2AlNb}$ and $E_{TiO_2}$ are the total energies of the two separated slabs, respectively, and $A$ is the interface area. The larger the $W_{sep}$ is, the more stable the interface will be. The work of separation can indicate the energy required to separate the $TiO_2$ scale and $Ti_2AlNb$ matrix.

Fig. 7(a) shows the relationship between the work of separation and interfacial spacing. With the increase of interfacial spacing, the work of separation will first increase and then

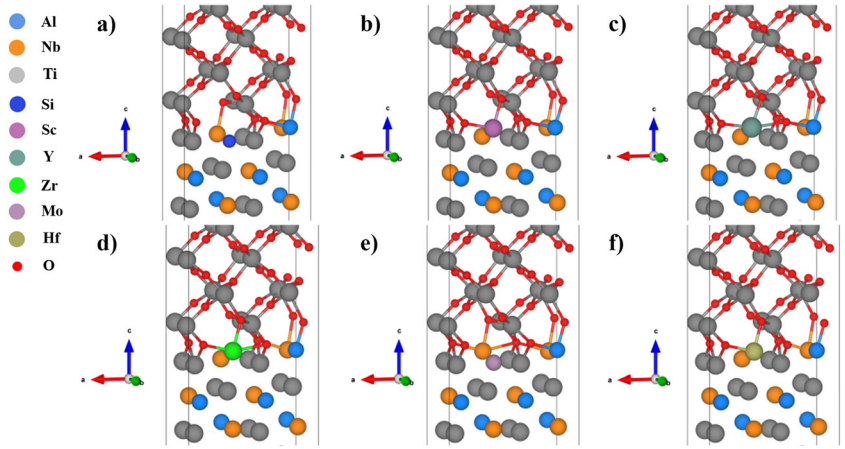


Fig. 4 Structures of the $TiO_2/Ti_2AlNb$ interface (Al substituted): (a) Si, (b) Sc, (c) Y, (d) Zr, (e) Mo, and (f) Hf.

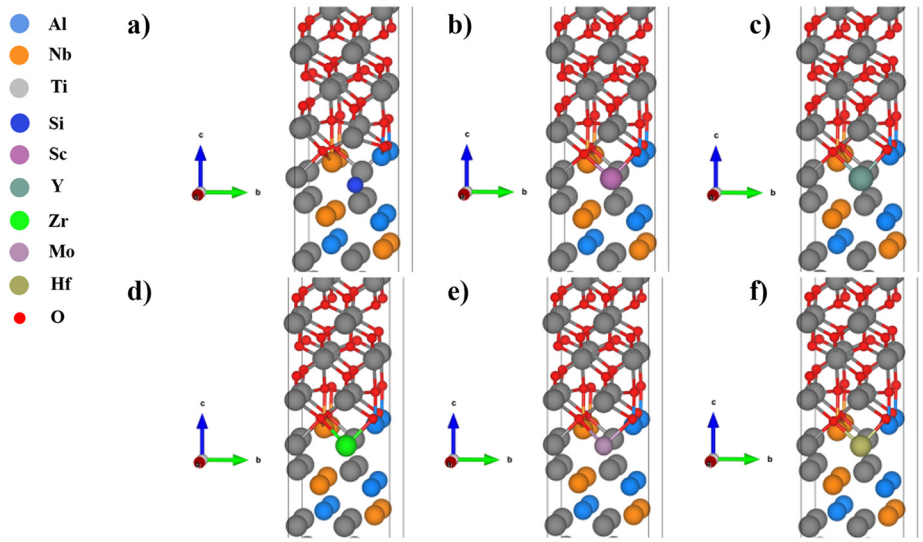


Fig. 5 Structures of the $TiO_2/Ti_2AlNb$ interface (Ti substituted): (a) Si, (b) Sc, (c) Y, (d) Zr, (e) Mo, and (f) Hf.

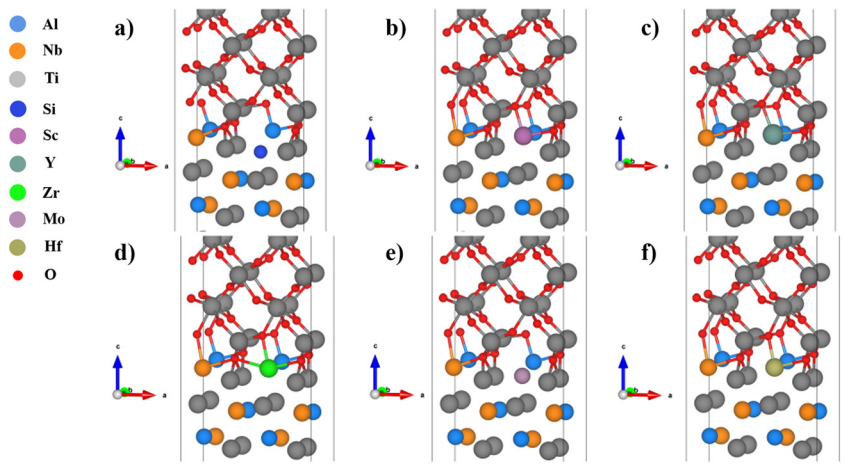


Fig. 6 Structures of the $TiO_2/Ti_2AlNb$ interface (Nb substituted): (a) Si, (b) Sc, (c) Y, (d) Zr, (e) Mo, and (f) Hf.

 

Table 3 Effect of alloying elements on the bond length in the $TiO_2$/$Ti_2AlNb$ interface

| | O–Al (Å) | O–Ti (Å) | O–Nb (Å) |
|---|---|---|---|
| Original | 1.96 | 2.08 | 2.36 |
| Al substituted | | | |
| | O–X (Å) | O–Ti (Å) | O–Nb (Å) |
| Si | — | 2.04 | 2.27 |
| Sc | 2.11 | 2.08 | — |
| Y | 2.22 | 2.08 | — |
| Zr | 2.16 | 2.09 | — |
| Mo | — | 2.06 | 2.20 |
| Hf | 2.11 | 2.09 | — |
| Ti substituted | | | |
| | O–Al (Å) | O–X (Å) | O–Nb (Å) |
| Si | 1.85 | — | 2.20 |
| Sc | 1.97 | 2.11 | 2.33 |
| Y | 1.96 | 2.24 | 2.32 |
| Zr | 1.92 | 2.23 | 2.14 |
| Mo | 1.87 | 2.24 | 2.10 |
| Hf | 1.96 | 2.14 | 2.35 |
| Nb substituted | | | |
| | O–Al (Å) | O–Ti (Å) | O–X (Å) |
| Si | 1.89 | 2.06 | — |
| Sc | 1.99 | 2.10 | 2.15 |
| Y | 2.01 | 2.10 | 2.28 |
| Zr | 1.98 | 2.08 | 2.30 |
| Mo | 1.95 | 2.09 | — |
| Hf | 1.98 | 2.09 | 2.20 |

decrease. The separation work is the largest, 4.84 J $m^{-2}$, at the equilibrium position, indicating that $TiO_2$ and $Ti_2AlNb$ have the best adhesion ability. To estimate the bonding stress in the normal direction of the interface, the partial derivative of the work of separation with the interfacial spacing is applied. (We process the data based on the numerical differentiation method of Origin6.0.)

$$\sigma = \left| -\frac{\partial W_{\text{sep}}}{\partial d} \right| \tag{5}$$

When the distance of normal separation is from 0 Å to −0.4 Å, the interface is subject to compression and the stress is negative, and therefore the absolute value of the calculation results is taken. Fig. 7(b) is the stress–strain curve. The strain is defined as the ratio of the movement distance to the original interface distance. When the strain is negative, the separation stress is also negative indicating a compressive stress state. The relationship between the stress and strain is basically linear. When the strain is greater than 0, the separation stress first increases linearly as the strain increases. When the strain approaches 1.46%, the stress continues to grow but the slope decreases. The adhesion strength of the interface is mainly affected by the bonding characteristics at the interface. In this interface model, the oxygen atoms of $TiO_2$ at the interface form bonds with the three metal atoms of $Ti_2AlNb$. The main bonding types of oxides are ionic bonds and covalent bonds, which are sensitive to changes in the bond length. When

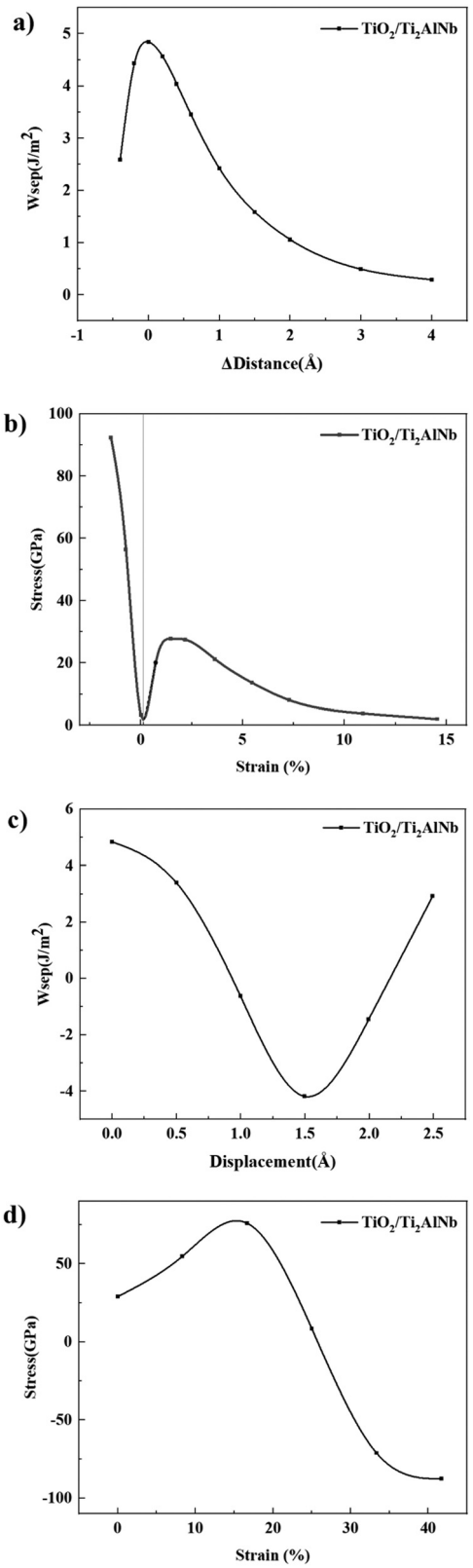


Fig. 7 (a) $W_{\text{sep}}$–distance curve and (b) stress–strain curve of the normal separation process of the $TiO_2$/$Ti_2AlNb$ interface. (c) $W_{\text{sep}}$–distance curve and (d) stress–strain curve of the tangential separation process of the $TiO_2$/$Ti_2AlNb$ interface.

the separation distance is small, small changes in the bond length can cause large stress changes. When the strain approaches 1.46%, the bonds between the oxygen and metallic ions are gradually stretched. When the strain increases from 1.46% to 2.5%, the bonds are gradually destroyed, and the change in stress value is small. When the strain exceeds 2.5%, most of the bonds are greatly weakened, and the adhesion strength will be mainly affected by the weak forces such as van der Waals, and the stress begins to decrease. The stress will gradually decrease resulting in further separation, which indicates the spalling of the $TiO_2$ scale. As the strain continues to increase, the stress continues to decrease slowly and gradually approaches zero. To explore the tangential separation behavior of the $Ti_2AlNb/TiO_2$ interface, the $TiO_2$ part is moved along the $\langle 010 \rangle$ direction of the interface model. Similar to the normal separation, the rigid shift method is adopted during simulations.[42,43] The total shear distance is selected as 2.49 Å, and the movement is divided into 5 steps with a step size of 0.49 Å. First, the work of separation ($W_{sep}$) is calculated according to eqn (3), and the work of separation–shear distance curve is shown in Fig. 7(c).

It can be seen that the work of separation is the largest near the equilibrium position. As the shear distance increases, the work of separation first decreases and then increases. This shows that the interface is the most stable at the equilibrium position and is not easily destroyed. As the distance changes, the stability of the interface decreases and it becomes easy to separate. This is mainly related to the change in the bonding interactions at the interfacial zone.

The shear stress is estimated from the partial derivative of the work of separation with the shuffling strain using the following formula:[44] (We process the data based on the numerical differentiation method of Origin6.0.)

$$F = -\frac{\partial W_{sep}}{\partial d} \tag{6}$$

Due to the tangential separation process, even if the direction of movement does not change, the stress may be in different directions because the oxygen–metal bond is stretched or compressed. Therefore, unlike the normal separation process, the absolute value of the results are not taken. As shown in Fig. 7(d), the stress first shows an upward trend and reaches the largest value when the strain reaches 16.7% with the increase of shear strain. The stress then decreases rapidly, reaching the lowest at a shear distance of 2.49 Å. It can be seen from the changing trend that when the strain reaches 16.7%, a larger stress is required to destroy the bond between oxygen and metallic atoms. After this point, the oxygen–metal bond is destroyed and the stress decreases rapidly.

Fig. S2(a) (ESI†) shows the changes in $W_{sep}$ with interface spacing of the Al substituted system. As the interface spacing changes, the separation work first increases and then decreases. When the interface model is compressed, the stability decreases rapidly and the interface is easily destroyed. $W_{sep}$ decreases with the increase of the interface spacing, indicating that the interface stability is gradually destroyed during the normal separation process. Compared with the alloying element containing systems, it can be seen that the change trends are basically similar and consistent with the original system. Near the equilibrium spacing, the $W_{sep}$ of the alloying system is changed in the order of Hf, Sc, Zr, Mo, Si and Y. Only the $W_{sep}$ of the Hf-doped system is slightly higher than that of the original system. The $W_{sep}$ of the Sc, Zr, and Mo systems is slightly smaller than that of the original system, and the $W_{sep}$ of the Si and Y systems is the smallest. Alloying elements slightly reduce the interface stability, and the Si and Y elements show greater effects due to their different atomic radii. Fig. S2(b) (ESI†) shows the change in stress with strain. The change trends of alloyed systems are basically similar. When the strain exceeds 0.73%, the growth rate of stress in each system gradually decreases and changes from linear growth to nonlinear. When the strain reaches 1.46%, the stress reaches the largest value. Then the stress remains at a high level within a certain strain range, which is the tension of the oxygen–metal bond. During the stretching and destruction processes, the stress generated is relatively large. After the strain exceeds 2.18%, the oxygen–metal bond is destroyed and the stress decreases rapidly and gradually approaches 0. Within the strain range of 1.46%–2.18%, the stress of the alloying system is changed in the order of Hf, Zr, Mo, Sc, Si and Y. The stress of the Hf doped system is the largest, which shows that the Hf element can strengthen the adhesion of the $TiO_2$ scale on $Ti_2AlNb$ and inhibit the spalling of the oxide. The stress of the Zr, Mo, and Sc alloyed systems is close to the original system.

Fig. S2(c) (ESI†) shows the $W_{sep}$ as a function of the interface spacing when the Ti substituted interface is separated normally. Near the equilibrium position, the $W_{sep}$ is changed in the order of Sc, Hf, Zr, Mo, Y and Si. The Sc element alloyed system is close to the original system, and the separation work of the other alloying systems is lower than that of the original interface. Therefore, the stability of the interface model is slightly reduced and the normal separation resistance is slightly weakened for substituted Ti systems. Among all studied systems, the Si-doped system has the lowest work of separation of 4.48 J $m^{-2}$. In the Ti substituted system, only the Si atom moved away from the original position and did not bond with oxygen. Among the other systems, the Sc-doped system has the highest $W_{sep}$, which is 4.84 J $m^{-2}$ near the equilibrium position. It is close to the original system. The differences in $W_{sep}$ between the substituted Ti systems and pure interface are larger than those of substituted Al systems, indicating that the O–Ti bond has a greater impact on the interface stability than the O–Al bond. This shows that the oxygen at the original interface prefers to combine with Ti. Fig. S2(d) (ESI†) shows the stress–strain curves of the studied systems. The compressive stress of each system shows a linear proportional relationship with the strain. For the positive strain, the stress first increases linearly with the increase of the interface spacing. When the strain exceeds 0.73%, the slope gradually decreases. For the strain in the range of 1.4% to 2.5%, the stress is maintained at a high level. The stresses within this range are arranged from high to low in the order of Sc, Hf, Zr, Mo, Y and Si.

Fig. S2(e) (ESI†) shows the calculation results of the $W_{sep}$ of the Nb substituted system. Near the equilibrium state, the work of separation of the alloyed systems changes in the order of Sc,

 

Hf, Zr, Y, Mo and Si. The $W_{sep}$ values of the Sc and Hf element containing systems are higher than that of the original system. The $W_{sep}$ of the Sc element system at the equilibrium position is 5.03 J $m^{-2}$, and the difference between the Hf, Zr, and Y element containing systems and the pure interface is small. The $W_{sep}$ values of the Mo and Si containing systems are lower than that of the pure interface system. The $W_{sep}$ of Si element at the equilibrium state is 4.48 J $m^{-2}$. In the Si and Mo alloyed systems, the Si and Mo atoms moved downward from the initial position, indicating the weak bonding interactions with oxygen atoms. This is the main reason for the weakening of the stability of the interface. Fig. S2(f) (ESI†) shows the stress–strain curves of alloyed systems. The largest normal stress is arranged from high to low in the order of Hf, Sc, Zr, Mo, Y and Si. Among them, the stress of the Hf element system is significantly higher than that of the pure interface system, followed by Sc and Zr elements. The difference between Mo and Y alloyed systems and the pure interface system is small in the strain range of 1.3% to 2.5%, while the stress of the Si element alloyed system is the smallest.

The effect of alloying elements on the tangential separation resistance of the $Ti_2AlNb/TiO_2$ interface was further calculated. Fig. S3(a) (ESI†) shows the results of the change in $W_{sep}$ with shear strain of the Al substituted interface systems. The change pattern of the curve is the same as that of the pure interface system. The $W_{sep}$ is at its largest value at the equilibrium state. The $W_{sep}$ increases with the shear strain; it first decreases and then increases. As tangential separation proceeds, the bonding state at the interface is changed and the stability decreases. When the shear movement exceeds 1 Å, the $W_{sep}$ of each system becomes negative. The interface will be easily destroyed. When the shear movement is around 1.5 Å, the interface model has an OT stacking structure, and the interface stability is the worst. The $W_{sep}$ changes in the order of Si, Y, Sc, Hf, Zr, and Mo. As shown in Fig. S3(b) (ESI†), as the strain increases, the stress first increases, reaching the highest value at a strain of 16.7%, and then decreases with a larger slope. When the strain reaches about 25%, the strain decreases to 0. Then with reverse growth, the strain reaches a turning point near 33.3%. When the strain is about 16.7%, the highest tangential stress is arranged in the order of Mo, Hf, Zr, Sc, Y and Si from high to low. The stress of the Mo element doped system is close to that of the original system, indicating that the Mo element has little effect on the tangential separation resistance of the interface model.

Fig. S3(c) (ESI†) shows the results of the $W_{sep}$ changing with the shear distance of the Ti substituted systems. The $W_{sep}$ first decreases and then increases as the shear distance increases. The $W_{sep}$ of alloyed systems is the largest at the equilibrium. When the shear movement is around 1.5 Å, the interface model has an OT stacking structure, and the interface stability is the worst. Fig. S3(d) (ESI†) shows the shear stress–strain curve. The stress first rises and reaches the highest value near the strain of 16.7% and then decreases rapidly. Comparing various systems, the largest stress of all alloyed systems is smaller than that of the pure interface system, which weakens the tangential separation resistance of the interface. The order from high to low is Sc, Hf, Y, Zr, Mo and Si.

As shown in Fig. S3(e) (ESI†), when the shear movement is 1.5 Å, the $W_{sep}$ of Nb substituted systems is arranged in the order of Si, Mo, Y, Sc, Hf and Zr from high to low. The $W_{sep}$ is higher than that of the pure interface system. Fig. S3(f) (ESI†) shows the change of stress with strain. The stress values near the strain of 16.3% from high to low are in the order of Zr, Hf, Sc, Y, Mo and Si. The lowest stress of each alloying system is lower than that of the original system, indicating that alloying slightly reduces the resistance of the tangential separation of the interface model.

### 3.3 Adhesion mechanism

The Nb substituted systems are more stable than Ti and Al substituted systems during the normal separation process as shown above. The Si alloyed system has the lowest work of separation, while the Hf alloyed system has the highest stress. Four systems with strains of 0%, 0.73%, 1.46% and −0.73% were selected for structural analysis. The bond lengths and structures are shown in Table 4 and Fig. 8 and 9 respectively.

For the Si alloyed system, when the strain is 0, the O–Al bond and O–Ti bond are 1.89 Å and 2.06 Å respectively. Since the Si atoms move downward, the Si atom does not bind with the oxygen atoms, and hence the Si alloyed system is less stable than the other systems and has the lowest $W_{sep}$. When the strain is −0.73%, the compressive stress increases rapidly, and the O–Al bond and O–Ti bond are shortened to 1.74 Å and 1.94 Å respectively. When the strain is 0.73%, the O–Al bond and O–Ti bond are stretched to 1.95 Å and 2.20 Å, respectively. Although the oxygen atoms of the subsurface of $TiO_2$ no longer bond with the Al atoms of $Ti_2AlNb$, the surface oxygen atoms are still well bonded with the metal atoms of $Ti_2AlNb$, and the tensile stress increases linearly. When the strain increases to 1.46%, the O–Al bonds and O–Ti bonds at the interface are stretched and begin to break (the O–Al bond length in the actual oxide $Al_2O_3$ is about 1.75 Å to 2.19 Å, and the O–Ti bond length in the main oxides of Ti, such as TiO and $TiO_2$, is about 1.78 Å to 2.34 Å). The interface model is subject to the highest normal stress. After the strain exceeds 2.5%, the bond fracture stress decreases rapidly. In the Hf alloyed system, as shown in Fig. 9, the Hf atom basically maintains the initial position. At the equilibrium state, the O–Al bond, O–Ti bond and O–Hf bond are 1.98 Å, 2.09 Å and 2.20 Å,

Table 4 Bond length changes during the normal separation process of the Si and Hf element doped (Nb substituted) $TiO_2/Ti_2AlNb$ interface

| Alloying elements | Strain (%) | O–Al (Å) | O–Ti (Å) | O–X (Å) |
|---|---|---|---|---|
| Si | −0.73 | 1.74 | 1.94 | — |
| | 0 | 1.89 | 2.06 | — |
| | 0.73 | 1.95 | 2.20 | — |
| | 1.46 | 2.02 | 2.35 | — |
| Hf | −0.73 | 1.80 | 1.95 | 2.00 |
| | 0 | 1.98 | 2.09 | 2.20 |
| | 0.73 | 2.04 | 2.24 | 2.37 |
| | 1.46 | — | — | — |

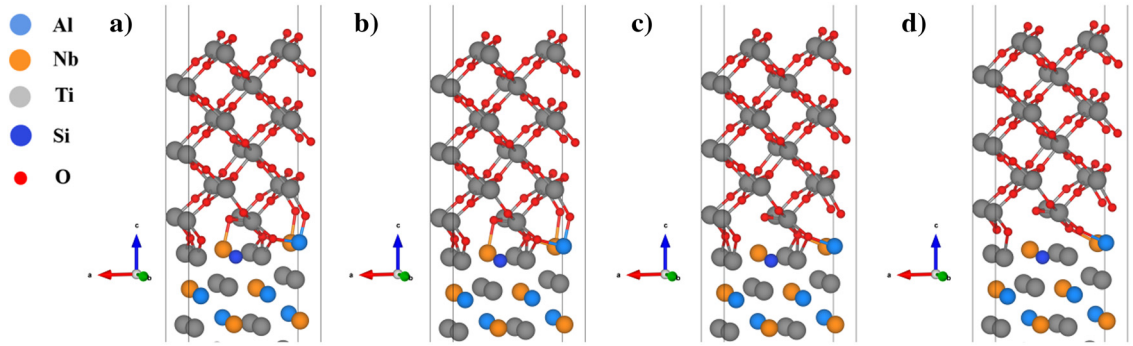


Fig. 8 Normal separation process of the Si element doped (Nb substituted) $TiO_2/Ti_2AlNb$ interface: (a) a strain of −0.73%, (b) a strain of 0%, (c) a strain of 0.73%, and (d) a strain of 1.46%.

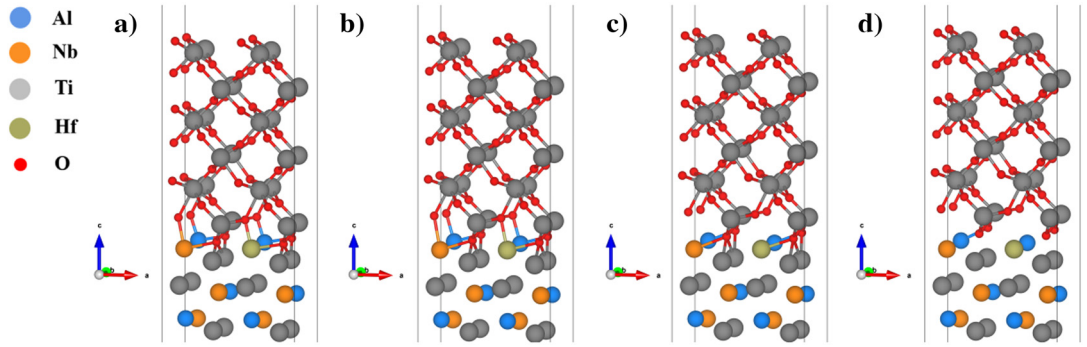


Fig. 9 Normal separation process of the Hf element doped (Nb substituted) $TiO_2/Ti_2AlNb$ interface: (a) a strain of −0.73%, (b) a strain of 0%, (c) a strain of 0.73%, and (d) a strain of 1.46%.

respectively. Compared with the Si alloyed system, the oxygen atom is better bonded with Hf. These are the main reasons for changes in stability and adhesion properties.

Fig. S4–S6 (ESI†) respectively show the differential charge changes of the interface during the normal separation process of the bare $TiO_2/Ti_2AlNb$ interface, the Si element doped (Nb substituted) $TiO_2/Ti_2AlNb$ interface and the Hf element doped (Nb substituted) $TiO_2/Ti_2AlNb$ interface. In the bare interface, the oxygen atoms in the bottom layer and sub-bottom layer of $TiO_2$ have obvious electron gain, and the metal atoms in the $Ti_2AlNb$ part have obvious electron loss around them, indicating strong bonding between oxygen and metal atoms. When the strain increases to 1.46%, there is still obvious electron transfer. However, the equivalent spherical surface decreases, indicating that the oxygen–metal bond begins to break, and the stress reaches the highest value at this strain. When the strain increases to 3.65%, the electron transfer trend decreases significantly, especially the electron gain from the oxygen atoms in the sub-layer decreases significantly. At this strain, some oxygen–metal bonds have been broken, and the stress begins to decrease. When the strain reaches 7.3%, there is only a small amount of charge transfer around the underlying oxygen atoms. At this strain, most of the oxygen–metal bonds are stretched and broken, and the stress further decreases. For the Si element doped $TiO_2/Ti_2AlNb$ interface, there is always no obvious electron gain or loss around Si atoms, indicating that Si and oxygen atoms do not interact with each other. This is the main reason for its poor adhesion strength. In contrast, the charge transfer near Hf atoms is obvious, indicating the strong bonding interactions between Hf and oxygen, which improve the adhesion strength of the $TiO_2/Ti_2AlNb$ interface. The density of states of alloyed systems was further calculated, as shown in Fig. 10. In the pure interface system, the p electrons of the oxygen atom appear as a bonding peak near −7.5 eV, overlapping with the d electrons of Ti and the d electrons of Nb respectively. In the Si doped system, the p electrons of oxygen near −7.5 eV only overlap with the d electrons of Ti, and there is no hybridization phenomenon with Si. Oxygen does not form a bond with Si. This is the reason for the small work of separation and weak adhesion properties of the Si alloyed system. In the Mo alloyed system, the p electrons of oxygen interact weakly with the d electrons of Mo. Similar to the Si alloyed system, the work of separation is high and the interface adhesion performance is weak. In contrast, the Sc, Zr, and Hf alloyed systems have obvious bonding interactions between alloying elements and oxygen, and therefore, they have better stability and interface adhesion properties, which may help to inhibit $TiO_2$ spalling and enhance the oxidation resistance properties.

We also used first-principles molecular dynamics calculation methods to analyze the structural stability of the interface at 1100 K with the NVT ensemble. After the simulation under

 

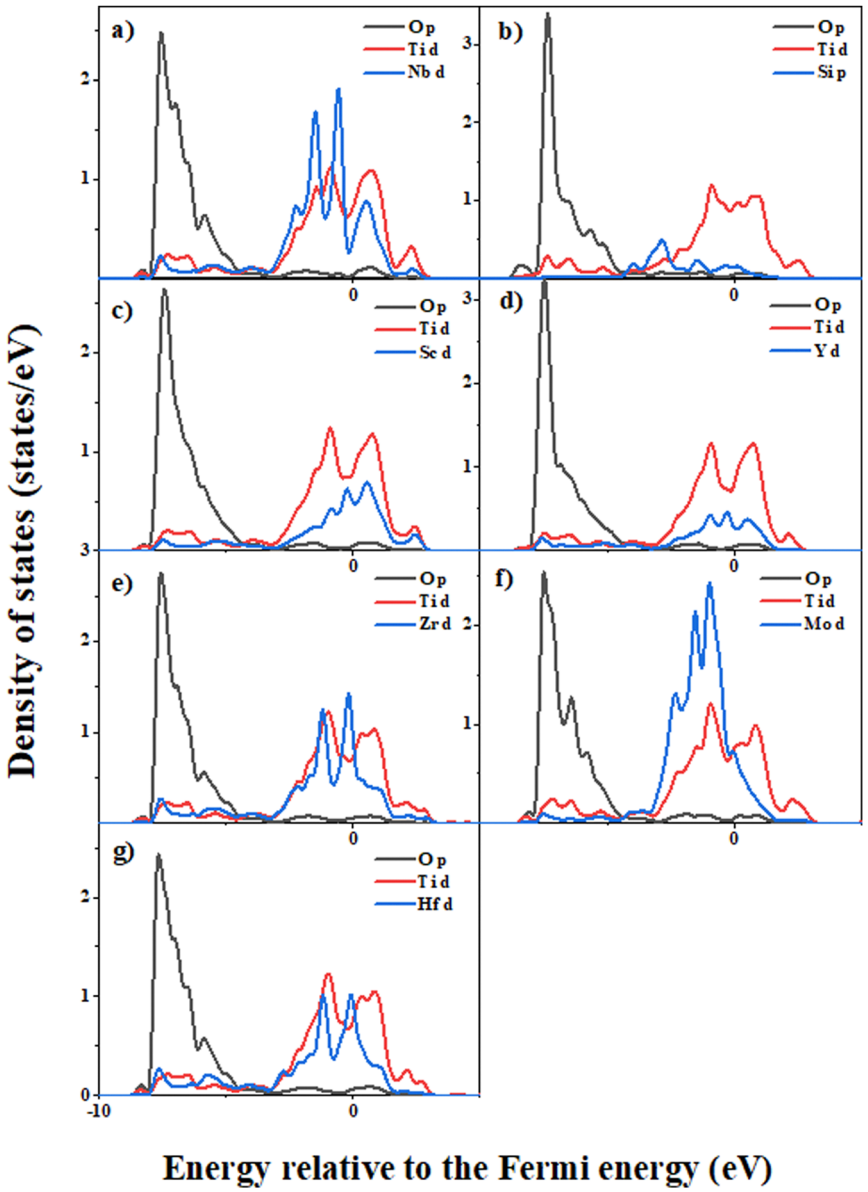


Fig. 10 Partial wave state density of oxygen atoms and the surrounding atoms at the interface: (a) the original system, (b) Si doped system, (c) Sc doped system, (d) Y doped system, (e) Zr doped system, (f) Mo doping system, and (g) Hf doped system.

5000 fs with the timestep of 1 fs, the energy convergence process and the interface structure after relaxation are shown in Fig. S7 and S8 (ESI†). Generally, the three interfaces all maintained their original structural characteristics after relaxation. First, in the bare $TiO_2$/$Ti_2AlNb$ interface, the oxygen atoms at the interface positions were bonded to the three metal atoms respectively, and almost no distortion occurred. In the Si element doped $TiO_2$/$Ti_2AlNb$ interface, the Si atom does not bond with oxygen, forming a large gap at the interface position, which may weaken the adhesion strength of the interface. In the Hf element doped $TiO_2$/$Ti_2AlNb$ interface, after relaxation, the Hf atom moves to the $TiO_2$ part and forms bonds with multiple nearby oxygen atoms. The good bonding state between Hf and oxygen atoms is the main reason why Hf strengthens the interface adhesion.

## 4. Conclusion

$Ti_2AlNb$ has excellent mechanical properties and good oxidation resistance, but the insufficient oxidation resistance properties hinder its potential application in the aerospace industry. The oxide scales easily spall under high temperature and stress conditions. First principles calculations have been employed to study the bonding interactions between $TiO_2$ and $Ti_2AlNb$, and the influence of alloying elements on the separation energy and tensile and shear deformations of the $TiO_2$/$Ti_2AlNb$ interface is studied in detail. The following results can be achieved *via* this study.

(1) The $TiO_2$/$Ti_2AlNb$ interface model is established. The HCP stacking structure interface is the most stable, in which the oxygen atoms of $TiO_2$ at the interface form bonds with the Al, Ti, and Nb atoms of the $Ti_2AlNb$ surface, respectively.

(2) Si, Sc, Y, Zr, Mo and Hf can exist stably at the $TiO_2$/$Ti_2AlNb$ interface. The Si and Mo elements have a great tendency to move into the interior of $Ti_2AlNb$, while the other alloying elements prefer to occupy their original positions. Alloying elements cause a certain degree of distortion, but have a less impact on interface stability.

(3) The effects of alloying elements on the adhesion properties of the $TiO_2$/$Ti_2AlNb$ interface were explored. During the normal separation process, the resistance mainly acts on the breaking of the oxygen–metal bond. In the Al substituted systems, Zr, Mo, and Hf elements improve the adhesion properties of $TiO_2$ on $Ti_2AlNb$. The Sc, Zr, and Hf elements strengthen the adhesion properties of $TiO_2$ in the Nb substituted systems.

Considering the requirement of specific strength of $Ti_2AlNb$, the selection of alloying elements should be done with caution. The Hf element has the highest mass density, the Zr element is close to the Nb element, while the Sc element has the lightest mass and is close to the Ti element. Therefore, from the perspective of the application in aero-engine parts and improving the engine thrust-to-weight ratio, the Zr and Sc elements are ideal. They maintain the advantage of lightweight and can further strengthen the oxidation resistance of the $Ti_2AlNb$ alloy.

## Conflicts of interest

There are no conflicts to declare.

## References

1 Y. J. Wang, X. H. Wang, Y. F. Yang, X. Lan, Z. Zhang and H. Li, *Materials*, 2022, **15**, 6238.
2 W. Chen, J. W. Li, L. Xu and B. Lu, *Adv. Mater. Processes*, 2014, **05**, 23–27.
3 J. J. Dai, C. X. Sun, A. M. Wang, H. Zhang, S. Li and H. Zhang, *Corros. Sci.*, 2021, **184**, 109336.
4 G. L. Liu and Y. Li, *Acta Phys. Sin.*, 2012, **61**, 177101.
5 G. Kushagra, B. Chandan and S. Neha, *J. Mater. Sci.*, 2022, **57**, 19553–19570.
6 J. Yang, Y. Wang, J. H. Huang, W. Wang, Z. Ye and S. Chen, *J. Alloys Compd.*, 2018, **755**, 211–223.
7 J. Yang, Y. Wang, J. H. Huang, Z. Ye, X. Sun, S. Chen and Y. Zhao, *Appl. Surf. Sci.*, 2019, **475**, 906–916.
8 Z. K. Muhammad, F. Jesper, H. N. Per, K. Marthinsen, I. G. Ringdalen and A. Strandlie, *Comput. Mater. Sci.*, 2021, **192**, 110319.
9 W. Shao, Z. J. Shi, L. X. Rao, X. Xing, Y. Zhou and Q. Yang, *Appl. Surf. Sci.*, 2021, **563**, 150279.
10 J. Lu, K. Guan, P. G. Rao, Q. Zeng, J. Liu and Z. Feng, *Appl. Phys. A: Mater. Sci. Process.*, 2021, **127**, 125.
11 Z. J. Shi, S. Liu, Y. F. Zhou, X. Xing, X. Ren and Q. Yang, *J. Alloys Compd.*, 2019, **773**, 264–276.
12 Z. J. Shi, W. Shao, T. S. Hu, C. Zhao, X. Xing, Y. Zhou and Q. Yang, *J. Alloys Compd.*, 2019, **805**, 1052–1059.
13 S. L. Zhang, L. X. Rao, W. Shao, Q. He, X. Xing, Y. Zhou and Q. Yang, *Langmuir*, 2022, **38**, 15113–15120.
14 Z. Y. Bao and F. L. Shang, *Appl. Sci.*, 2022, **12**, 8869.
15 B. D. Wang, J. H. Dai, X. Wu, Y. Song and R. Yang, *Intermetallics*, 2015, **60**, 58–65.
16 Y. Song, F. J. Xing, J. H. Dai and R. Yang, *Intermetallics*, 2014, **49**, 1–6.
17 J. H. Dai, Y. Song and R. Yang, *Intermetallics*, 2017, **85**, 80–89.
18 Y. Li, J. H. Dai and Y. Song, *Comput. Mater. Sci.*, 2020, **181**, 109756.
19 A. V. Bakulin, S. S. Kulkov, A. A. Fuks and S. E. Kulkova, Tomsk, Russia, 2018.
20 H. N. Hao, X. Wang and F. H. Wang, Guangzhou, People's Republic of China, 2012.
21 A. Q. Wang, P. Liu, J. P. Xie, D. Ma and Z. Mao, *J. Alloys Compd.*, 2020, **817**, 152734.
22 Z. Z. Li, Y. Wei, H. B. Zhou and G. Lu, *Eur. Phys. J. B*, 2016, **89**, 280.
23 D. H. Li, B. B. Wang, L. S. Luo, X. Li, Y. Xu, B. Li, L. Wang, W. Liu, B. Han, Y. Su, J. Guo and H. Fu, *Mater. Sci. Eng., A*, 2021, **827**, 142095.
24 C. X. Zou, J. S. Li, L. Zhu, Y. Zhang, G. Yao, B. Tang, J. Wang, H. Kou, H. Song and W. Y. Wang, *Intermetallics*, 2021, **133**, 107173.
25 Y. Cao, T. Li, S. G. Zhou, Y. Xu, P. Wang, J. Liu, D. Zhang and J. Duan, *Mater. Today Commun.*, 2022, **32**, 104049.
26 Y. Li, J. H. Dai, Y. Song and R. Yang, *Comput. Mater. Sci.*, 2017, **139**, 412–418.
27 J. Chen, Q. Chen, S. J. Qu, H. P. Xiang, C. Wang, J. B. Gao, A. H. Feng and D. L. Chen, *Scr. Mater.*, 2021, **199**, 113852.
28 Z. C. Dong, A. H. Feng, H. Wang, S. Qu and H. Wang, *Metals*, 2023, **13**, 485.
29 A. J. Samin, *J. Alloys Compd.*, 2021, **879**, 160455.
30 G. Kresse and J. Furthmüller, *Phys. Rev. B: Condens. Matter Mater. Phys.*, 1996, **54**, 11169.
31 J. P. Perdew, K. Burke and M. Ernzerhof, *Phys. Rev. Lett.*, 1996, **77**, 3865–3868.
32 K. Hu, J. Huang, Z. Wei, Q. Peng, Z. Xie, B. Sa and B. Wu, *Phys. Status Solidi B*, 2017, **254**, 1600634.
33 W. Ruan, X. Zeng, H. Wan, W. Mei and Y. Wen, *Mater. Res. Express*, 2019, **6**, 096510.
34 G. Kresse and J. Furthmüller, *Comput. Mater. Sci.*, 1996, **6**, 15–50.
35 A. Banerjea and J. R. Smith, *Phys. Rev. B: Condens. Matter Mater. Phys.*, 1988, **37**, 6632–6645.
36 A. V. Bakulin, S. Hocker and S. E. Kulkova, *Phys. Mesomech.*, 2021, **24**, 523–532.
37 A. V. Bakulin, S. S. Kulkov, S. E. Kulkova, S. Hocker and S. Schmauder, *Metals*, 2020, **10**, 1298.
38 A. Ralison, F. Dettenwanger and M. Schutze, *Mater. High Temp.*, 2003, **20**, 607–629.
39 W. Dang, J. S. Li, T. B. Zhang and K. Hongchao, *Rare Met. Mater. Eng.*, 2015, **44**, 261–266.
40 M. Dade, V. A. Esin, L. Naze and P. Sallot, *Corros. Sci.*, 2019, **148**, 379–387.
41 V. Imayev, N. Parkhimovich, D. Trofimov and R. Imayev, *Lett. Mater.*, 2021, **11**, 524–530.
42 Z. K. Muhammad, F. Jesper, H. N. Per, K. Marthinsen and A. Strandlie, *Comput. Mater. Sci.*, 2021, **187**, 110058.
43 S. L. Zhang, L. X. Rao, W. Shao, Q. He, X. Xing, Y. Zhou and Q. Yang, *Diamond Relat. Mater.*, 2022, **130**, 109416.
44 G. Levita, E. Molinari, T. Polcar and M. C. Righi, *Phys. Rev. B: Condens. Matter Mater. Phys.*, 2015, **92**, 085434.

 